RSC Advances

PAPER

View Article Online
View Journal | View Issue

Cite this: *RSC Adv.*, 2017, 7, 13604

Highly efficient non-doped blue organic light emitting diodes based on a D–π–A chromophore with different donor moieties†

Venugopal Thanikachalam,* Palanivel Jeeva and Jayaraman Jayabharathi

Received 16th December 2016
Accepted 21st February 2017

DOI: 10.1039/c6ra28303a

rsc.li/rsc-advances

Comparative photophysical, electroluminance and theoretical investigations have been made for 4′-(1-(4-morpholinophenyl)-1*H*-phenanthro[9,10-*d*]imidazole-2-yl)-styryl-2-(4′-9*H*-carbazole-9-yl) (MPPIS-Cz) and 4′-(1-(4-morpholinophenyl)-1*H*-phenanthro[9,10-*d*]imidazole-2-yl)-styryl-*N*,*N*-diphenyl-[1,1′-biphenyl]-4-amine (MPPIS-TPA). Based on tuning the donor ability, MPPIS-TPA and MPPIS-Cz were designed to have a hybridized local and charge transfer state (HLCT) and a hot exciton channel. This HLCT is responsible for high photoluminescence efficiency and the hot exciton contributes to high exciton utilization. The non-doped OLED based on MPPIS-Cz exhibits excellent performance: blue emission with CIE coordinates of (0.16, 0.08), maximum current efficiency of 1.52 cd A^{-1} and maximum external quantum efficiency of 1.42%. A fluorescent molecule with a HLCT state and hot exciton may be an ideal strategy to design next generation, high efficiency and low cost fluorescent OLED materials.

Open Access Article. Published on 28 February 2017. Downloaded on 2/17/2026 6:30:33 PM.
This article is licensed under a Creative Commons Attribution 3.0 Unported Licence.

1. Introduction

Deep blue emitters with donor–π–acceptor geometry have been widely investigated in order to reduce power consumption in organic optoelectronics. The blue emitter with a wide band gap requires a limited π-conjugation length.[1–5] Simultaneous injection of electrons and holes into the blue emitter becomes very difficult due to its wide band gap and so the device efficiency is reduced.[6,7] High efficiency and low cost light emitting materials are urgent requirements for OLEDs. The external quantum efficiency (η_{EQE}) of devices can be calculated using: $\eta_{\text{EQE}} = \eta_{\text{IQE}} \times \eta_{\text{out}} = \eta_{\text{rec}} \times \eta_{\text{PL}} \times \eta_{\text{S}} \times \eta_{\text{out}}$, where η_{IQE} is internal quantum efficiency; η_{out} ($\sim 1/2n^2$) is light out coupling efficiency ($n = 1.5$, $\eta_{\text{out}} \sim 20\%$); η_{rec} is efficiency for electron–hole recombination (100%); η_{PL} is photoluminescence efficiency of a solid film and η_{S} is exciton utilization efficiency.[8] The two important parameters, η_{PL} and η_{S} can be adjusted by tuning the molecular design to enhance the external quantum efficiency (η_{EQE}).

The η_{PL} is related to radiative rate (k_r) and is directly proportional to transition dipolemoment which is enhanced by increasing the orbital overlap (high oscillator strength), indicative of locally excited (LE) state or extended π-conjugation. The CT state leads to enhance the reverse intersystem crossing (RISC) between singlet and triplet states ($\Delta E_{\text{ST}} \approx 0$).[9] Thus, CT state in electroluminescent (EL) materials will enable the triplet exciton utilization (η_{S}) in fluorescent OLEDs through RISC (T → S) process. But CT state is not an efficient radiative state as a result of spatial separation of transition orbitals.[10,11] Therefore, it is difficult to have high η_{PL} with high η_{S} in same fluorescent molecule interms of orbital overlap and excited state character. Construction of emissive state consists of both LE and CT state components to achieve high PL efficiency (from LE state) and high exciton utilization (from CT state) is of current interest.[12]

Organic donor–acceptor (D–A) compounds with hybridized local and charge transfer (HLCT) state exhibit high η_{S} in fluorescent OLEDs which can be attributed by hot exciton mechanism.[13–19] The low lying LE dominated HLCT state provides a high radiative rate for high η_{PL} whereas the high-lying CT dominated HLCT state is responsible for high η_{S} through RISC process along with hot exciton mechanism.[17–20] According to the energy gap law, the larger energy gap between T_2 and T_1 states greatly reduce the internal conversion (IC) ($T_2 \xrightarrow{k_{\text{IC}}} T_2$) results hot RISC ($T_2 \xrightarrow{k_{\text{RISC}}} S_1/S_2$) than cold RISC ($T_1 \rightarrow S_1$) in TADF mechanism.[21,22] Therefore, hot exciton mechanism with HLCT state increases the η_{EQE} as a result of coexistence of high η_{PL} and high η_{S}.

Based on the above issues, herein we report 4′-(1-(4-morpholinophenyl)-1*H*-phenanthro[9,10-*d*]imidazole-2-yl)-styryl-2-(4′-9*H*-carbazole-9-yl) (MPPIS-Cz) and 4′-(1-(4-morpholinophenyl)-1*H*-phenanthro[9,10-*d*]imidazole-2-yl)-styryl-*N*,*N*-diphenyl-[1,1′-biphenyl]-4-amine (MPPIS-TPA) shows high fluorescence efficiency. The strong donor triphenylamine (TPA) in MPPIS-TPA is replaced with a weaker electron donating carbazole (Cz) in MPPIS-Cz which is expected to decrease CT component with simultaneous increase of LE component in S_1 HLCT state.

Department of Chemistry, Annamalai University, Annamalainagar 608 002, Tamilnadu, India. E-mail: vtchalam2005@yahoo.com; Tel: +91 9488476098

† Electronic supplementary information (ESI) available. See DOI: 10.1039/c6ra28303a

This journal is © The Royal Society of Chemistry 2017

Open Access Article. Published on 28 February 2017. Downloaded on 2/17/2026 6:30:33 PM. This article is licensed under a Creative Commons Attribution 3.0 Unported Licence.

The η_{PL} of MPPIS-Cz film is enhanced compared to MPPIS-TPA film and thus combined effect of high η_{PL} and high η_S enhanced the η_{EQE} of MPPIS-Cz based device.

2. Experiment and characterization

Sigma-Aldrich supplied all the chemicals for the synthesis of blue emissive materials (Scheme S1†). The ^{1}H and ^{13}C NMR and mass spectra were obtained on Bruker 400 MHz NMR spectrometer and Agilent LCMS VL SD in electron ionization mode, respectively. Cyclic voltammetry (CV) analyses have been carried out to calculate HOMO energy of MPPIS-Cz and MPPIS-TPA by using CHI 630A potentiostat electrochemical analyzer with platinum electrode and platinum wire as the working electrode and counter electrode, respectively. The Ag/Ag$^+$ electrode is used as the reference electrode at a scan rate of 100 mV s^{-1} with 0.1 M tetrabutylammoniumperchlorate in CH$_2$Cl$_2$ as the supporting electrolyte. The UV-visible spectra were recorded using Perkin Elmer Lambda 35 UV-vis spectrophotometer and corrected for background absorption due to solvent. Perkin Elmer Lambda 35 spectrophotometer with RSA-PE-20 integrating sphere attachment was employed to record UV-vis diffuse reflectance spectra. Photoluminescence spectra were recorded on a Perkin Elmer LS55 fluorescence spectrometer. The PL quantum yield was calculated in dichloromethane with 0.5 M H$_2$SO$_4$ solution of quinine (0.54) as reference using the following equation: $\phi_{unk} = \phi_{std}\left(\frac{I_{unk}}{I_{std}}\right)\left(\frac{A_{std}}{A_{unk}}\right)\left(\frac{\eta_{unk}}{\eta_{std}}\right)^2$ where ϕ_{unk} and ϕ_{std} are the radiative quantum yield of the sample and standard, I_{unk} and I_{std} are the integrated emission intensities of the sample and standard, respectively. A_{unk} and A_{std} are the absorbances of the sample and standard, respectively and η_{unk} and η_{std} are the refractive indices of the sample and standard solutions. The solid state quantum yield has been measured on the quartz plate using an integrating sphere. Thermo gravimetric analyses (TGA) was carried out on a Perkin Elmer thermal analysis system at a heating rate of 10 °C min^{-1} with nitrogen flow rate of 100 mL min^{-1}. Differential scanning calorimetric (DSC) analysis was recorded with NETZSCH (DSC-204) at 10 °C min^{-1} under nitrogen atmosphere (100 mL min^{-1}).

2.1. Computational details

All the density functional theory (DFT) calculations were carried out using Gaussian 09 package.[23] The density functional theory (DFT) and time-dependent DFT (TD-DFT) were carried out for ground state and excited state geometry optimization at the level of B3LYP/6-31G (d, p). In order to examine the nature of electronic transitions for excited states, natural transition orbital (NTOs) are evaluated with the dominant particle–hole pair contributions and the associated weights.[23] The out file obtained from the TD-DFT method used to get transition property such as the electron–hole distribution, the overlap of electron–hole of excited states, natural transition orbital and transition density matrix and are analyzed with the multifunctional wave function analyzer (Multiwfn).[23]

2.1.1. 2-(4-Bromostyryl)-1-(4-morpholinophenyl)-1*H*-phenanthro[9,10-*d*]imidazole (BSMPPI). BSMPPI was synthesised by refluxing 9,10-phenanthrenequinone (5 mmol), 4-bromocinnamaldehyde (5 mmol), 4-morpholinobenzenamine (6 mmol) and ammonium acetate (61 mmol) in ethanol (20 mL) for 12 h under nitrogen atmosphere. The reaction mixture was cooled and extracted with dichloromethane. The extract was concentrated and the residue was purified by column chromatography (petroleum ether : CH$_2$Cl$_2$, 1 : 1). M. P. 246 °C. Anal. calcd for C$_{33}$H$_{27}$BrN$_3$O: C, 82.30; H, 5.65; Br, 14.83; N, 8.73. Found: C, 82.43; H, 5.68; Br, 14.78; N 8.71. ^{1}H NMR (400 MHz, CDCl$_3$): δ 3.19 (s, 4H), 3.48 (s, 4H), 6.64 (d, J = 8.8 Hz, 1H), 7.11 (d, J = 16.0 Hz, 1H), 7.19 (d, J = 8 Hz, 2H), 7.35–7.46 (m, 4H), 7.47–7.55 (m, 5H), 7.73 (d, J = 17.6 Hz, 1H), 7.82 (d, J = 16.8 Hz, 1H), 8.03 (d, J = 15.5 Hz, 2H), 8.51 (d, 2J = 14.6 Hz, H), 9.41 (t, 1H). ^{13}C NMR (100 MHz, CDCl3): δ 51.33, 69.42, 115.78, 120.53, 120.96, 121.41, 121.88, 122.22, 122.54, 123.95, 124.22, 124.95, 125.12, 125.80, 125.95, 126.27, 126.36, 126.49, 126.77, 127.09, 127.34, 127.43, 127.64, 128.82, 130.83, 132.35, 147.77. MS: m/z 481.6 [M$^+$]; calcd 481.81.

2.1.2. 4′-(1-(4-Morpholinophenyl)-1*H*-phenanthro[9,10-*d*] imidazole-2-yl)-styryl-2-(4′-9*H*-carbazole-9-yl) (MPPIS-Cz). A mixture of carbazole, 2-(4-bromostyryl)-1-(4-morpholinophenyl)-1*H*-phenanthro[9,10-*d*]imidazole (BSMPPI) (0.45 g, 1.0 mmol), CuI (10.0 mg, 0.05 mmol), 18-crown-6 (13.2 mg, 0.05 mmol), and K$_2$CO$_3$ (0.83 g, 6.0 mmol) in tetrahydro-1,3-dimethylpyrimidin-2(1*H*)-one (2.0 mL) was refluxed in nitrogen atmosphere for 18 h. The reaction mixture was cooled and extracted with dichloromethane. The extract was concentrated and the residue was purified by column chromatography (petroleum ether : CH$_2$Cl$_2$, 1 : 1). Mp 289 °C. Anal. calcd for C$_{45}$H$_{34}$N$_4$O: C, 83.57; H, 5.30; N, 8.66. Found: C, 83.46; H, 5.24; N, 8.61. ^{1}H NMR (400 MHz, CDC$_{l3}$): δ 3.14 (s, 4H), 3.43 (s, 4H), 6.53 (d, J = 16.0 Hz, 1H), 6.58 (d, J = 16.0 Hz, 1H), 6.97–7.13 (m, 5H), 7.16 (d, J = 16.2 Hz, 1H), 7.27–7.41 (m, 7H), 7.48 (s, 2H), 7.53 (d, J = 17.0 Hz, 1H), 7.87–7.94 (m, 4H), 8.07–8.11 (m, 3H), 8.67 (d, J = 14.2 Hz, 2H). ^{13}C NMR (100 MHz, CDC$_{l3}$): δ 53.68, 71.36, 102.08, 111.28, 113.67, 116.12, 120.08, 121.26, 121.47, 122.58, 122.67, 122.89, 126.07, 126.22, 126.43, 126.87, 126.91, 129.78, 131.82, 132.13, 134.71, 138.36, 140.83, 148.24. MALDI-TOF MS: m/z 645.7 [M$^+$], calcd 646.8.

2.1.3. 4′-(1-(4-Morpholinophenyl)-1*H*-phenanthro[9,10-*d*] imidazole-2-yl)-styryl-*N*,*N*-diphenyl-[1,1′-biphenyl]-4-amine (MPPIS-TPA). A mixture of 2-(4-bromostyryl)-1-(4-morpholinophenyl)-1*H*-phenanthro[9,10-*d*]imidazole (BSMPPI) (4.5 mmol), 4-(diphenylamino)phenylboronic acid (7.5 mmol), Pd(PPh$_3$)$_4$ (0.25 mmol) and aqueous Na$_2$CO$_3$ (15 mL) in toluene : ethanol (20 : 15 mL) was refluxed in nitrogen atmosphere for 18 h. The reaction mixture was cooled and extracted with dichloromethane. The extract was concentrated and the residue was purified by column chromatography (petroleum ether : CH$_2$Cl$_2$, 1 : 1). Mp 275 °C. Anal. calcd for C$_{51}$H$_{40}$N$_4$O: C, 84.50; H, 5.56; N, 7.73. Found: C, 84.32; H, 5.36; N, 7.57. ^{1}H NMR (400 MHz, CDCl$_3$): δ 3.27 (s, 4H), 3.54 (s, 4H), 6.69 (s, 2H), 6.98–7.23 (m, 8H), 7.33–7.49 (m, 11H), 7.57 (d, J = 16.8 Hz, 1H), 7.64 (d, J = 18.2 Hz, 1H), 7.98–8.06 (m, 6H), 8.22 (d, J = 17.4 Hz, 1H), 8.79 (s,

Open Access Article. Published on 28 February 2017. Downloaded on 2/17/2026 6:30:33 PM.
This article is licensed under a Creative Commons Attribution 3.0 Unported Licence.

2H). ^{13}C NMR (100 MHz, CDCl$_3$): δ 55.72, 73.47, 106.58, 115.32, 117.92, 120.42, 124.87, 125.39, 125.61, 126.43, 126.61, 126.87, 130.32, 130.77, 130.98, 134.73, 136.92, 138.84, 139.91, 142.34, 151.26. MALDI-TOF MS: *m*/*z* 723.7 [M$^+$], calcd 724.9.

3. Results and discussion

3.1. Donor–π–acceptor molecular design

4′-(1-(4-Morpholinophenyl)-1*H*-phenanthro[9,10-*d*]imidazole-2-yl)-styryl-2-(4′-9*H*-carbazole-9-yl) (MPPIS-Cz) is composed of carbazole (Cz) as electron donor and morpholinophenylphenanthrimidazole as electron acceptor with styryl as spacer. To improve photoluminance efficiency (η_{PL}), the strong electron donor TPA moiety in MPPIS-TPA is replaced with weaker donor moiety Cz to decrease the CT component with increase of LE component in the emissive S$_1$ state of MPPIS-Cz. The ground state (S$_0$) and excited state (S$_1$) geometries were optimized using DFT/B3LYP/6-31G (d, p) and TD-DFT/B3LYP/6-31G (d, p) methods for MPPIS-Cz and MPPIS-TPA (Fig. 1). The three key twist angles (TA) exist in MPPIS-TPA and MPPIS-Cz are: θ_1 – between phenanthrimidazole plane and styryl at C2) N1-TA, θ_2 – between phenanthrimidazole plane and 4-morpholinobenzenamine at N1 and θ_3 – between biphenyl fragment in MPPIS-TPA and between styryl phenyl and carbazole ring MPPIS-Cz. In ground state the styryl fragment (θ_1) and 4-morpholinobenzenamine (θ_2) are highly twisted about phenanthrimidazole plane with dihedral angle of θ_1 – 36°; θ_2 – 73° for MPPIS-TPA and θ_1 – 61°; θ_2 – 75° for MPPIS-Cz. The TPA moiety in MPPIS-TPA and Cz moiety in MPPIS-Cz also twisted with dihedral angles of 47° and 45°, respectively.[24a] The larger twist angle of MPPIS-Cz when compared with MPPIS-TPA is due to the stronger repulsion between the two adjacent hydrogen atoms in carbazole and phenyl ring, as a result of the stronger rigidity of Cz than TPA. The excited state twist angle θ_1 of MPPIS-Cz and MPPIS-TPA are increased to 74.15° and 42.56°, respectively, when compared with ground state twist angle θ_1. Similarly smaller twist angle θ_2 was obtained for MPPIS-Cz when compared with MPPIS-TPA. The bond length (R_1) of MPPIS-Cz and MPPIS-TPA are elongated by 0.02 and 0.07 Å, respectively from S$_0$ to S$_1$. The observed smaller change of geometry from S$_0$ to S$_1$ in Cz moiety of MPPIS-Cz than that of TPA unit in MPPIS-TPA may decrease the non radiative emission (k_{nr}) results enhancement of photoluminance efficiency.

The highest occupied molecular orbital (HOMO) and the lowest unoccupied molecular orbital (LUMO) are mainly localized on Cz (MPPIS-Cz) and TPA (MPPIS-TPA) and MPPIS moieties, respectively (Fig. 2). This bipolar molecular design with the balanced carrier transport property is an additional benefit of MPPIS-Cz and MPPIS-TPA molecules as the light emitting layer in which Cz (MPPIS-Cz) and TPA (MPPIS-TPA) acts as hole-

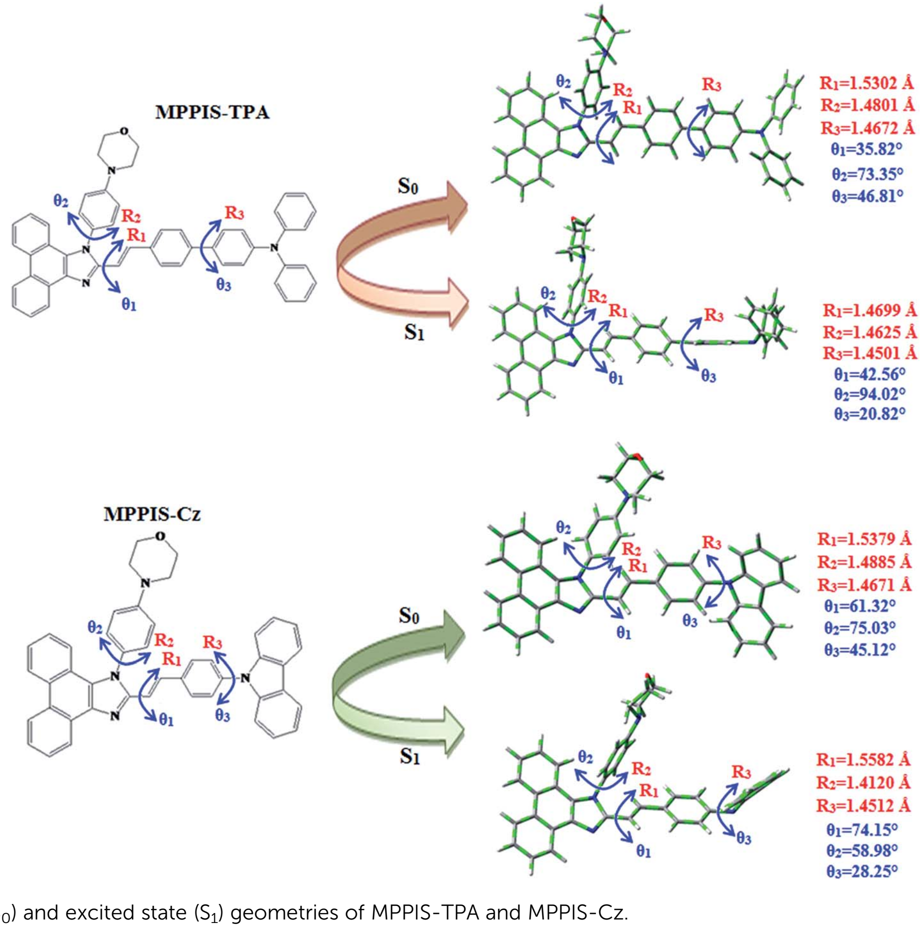

Fig. 1 Ground state (S$_0$) and excited state (S$_1$) geometries of MPPIS-TPA and MPPIS-Cz.

Open Access Article. Published on 28 February 2017. Downloaded on 2/17/2026 6:30:33 PM. This article is licensed under a Creative Commons Attribution 3.0 Unported Licence.

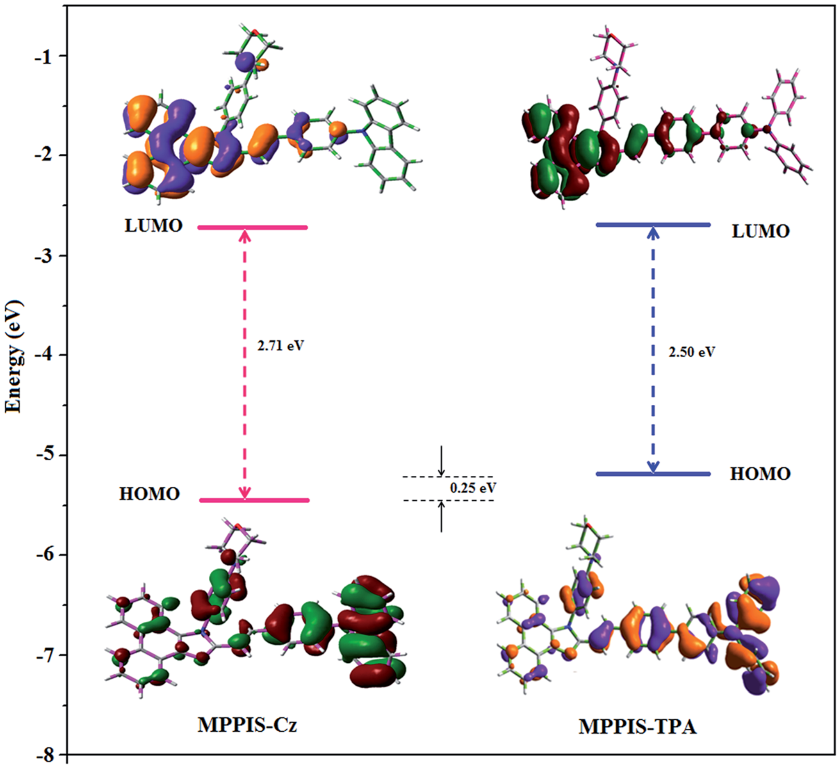

Fig. 2 HOMO and LUMO contour map of MPPIS-Cz and MPPIS-TPA.

transporting group and MPPIS as electron transporting group, respectively. Compared with MPPIS-TPA, the delocalization of HOMO decreases in MPPIS-Cz indicating that the Cz is a weak donor than TPA. The HOMO energy of MPPIS-Cz is decreased by 0.25 eV compared to that of MPPIS-TPA corresponding to the weak electron donating ability of Cz than TPA.

To understand the nature of excited states, the natural transition orbitals (NTO)[24] of MPPIS-Cz and MPPIS-TPA have been analyzed (Fig. 3). For S_1 and S_2 states, NTO hole and particle distribution in MPPIS-Cz are almost similar to those in MPPIS-TPA. The hole is delocalized over entire molecular backbone whereas particle is localized on MPPIS and styryl fragments. However, similar particle contour is obtained in both MPPIS-Cz and MPPIS-TPA, the hole contour of MPPIS-Cz is shrunk as a result of weaker donor ability of Cz. This indicates an enhanced LE component in S_1 state HLCT. The oscillator strength of S_1 state of MPPIS-Cz (0.7557) is higher than that of MPPIS-TPA (0.6148) results higher η_{PL} for MPPIS-Cz than for MPPIS-TPA (Table S1†). Chemical modification from TPA to Cz induces an increase LE component in S_1 emissive state together with rigid molecular skeleton. Both S_1 and S_2 states exhibit a character of hybridized local and charge transfer state (HLCT) in which higher LE character of S_1 state enhance the η_{PL} in MPPIS-Cz. The hole contour on Cz or TPA moiety are in the opposite phase between S_1 and S_2 states whereas the particle on MPPIS moiety is same between S_1 and S_2 states for MPPIS-Cz and MPPIS-TPA, respectively. This implied that the interstate hybridization coupling occurs through the positive and negative linear combination between LE and CT state wave function: $\Psi_{S_1/S_2} = c_{LE}\Psi_{LE} \pm c_{CT}\Psi_{CT}$. The percentage of pure CT level of MPPIS-Cz (~10%) is less than that of MPPIS-TPA (~20%) as a result of the weak donor ability of Cz than TPA leading to LE dominated S_1 state in MPPIS-Cz (LE ~ 90%) and LE/CT balanced S_1 state in MPPIS-TPA (LE ~ 80%). As a result MPPIS-Cz should exhibit higher photoluminance efficiency (η_{PL}) and blue shifted emission relative to MPPIS-TPA.

The singlet state energies have been estimated at the geometry of S_0 state. A large energy gap occurs between T_1 and T_2 for both MPPIS-Cz and MPPIS-TPA arising from the same MPPIS acceptor group and the energy gap between T_1 and T_2 of MPPIS-Cz is larger than MPPIS-TPA (Fig. 4a).[25,26] A very small ΔE_{ST} is observed between S_1 and T_2 states facilitating RISC ($T_2 \rightarrow S_1$) process in both MPPIS-Cz and MPPIS-TPA as a result of their HLCT state character (Fig. 4b). Thus, compared with MPPIS-TPA, MPPIS-Cz can be expected to obtain high photoluminance efficiency (η_{PL}) and high exciton utilisation efficiency (η_S) and further to enhance the external quantum efficiency (η_{EQE}) of the fluorescent OLED as a result of increased LE component in S_1 state.

The eigen value for all states is greater than 0.98 which also indicate that the better mixed excited state can be described in terms of dominant excitation pair according to 98% of the transition which is further supported by overlap integral (Δr index – eqn (S1)) which is greater than two for all singlet and triplet states of MPPIS-TPA and less than two for MPPIS-Cz (Table S2†). The Δr index measures the average hole–electron distance upon excitation and it is related to the nature of the excitation type (LE or CT) since valence excitation (LE) is

Open Access Article. Published on 28 February 2017. Downloaded on 2/17/2026 6:30:33 PM.
This article is licensed under a Creative Commons Attribution 3.0 Unported Licence.

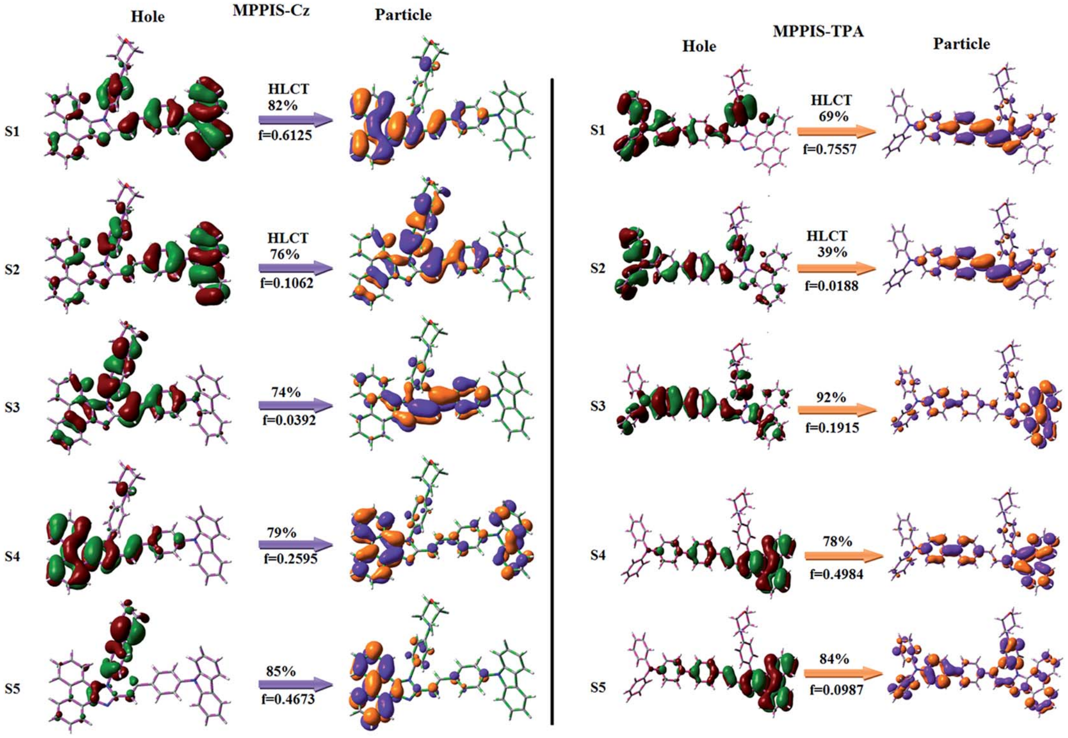

Fig. 3 Computed natural transition orbital pairs for S_1–S_5 of MPPIS-Cz and MPPIS-TPA [oscillator strength (*f*): percentage weights of hole–particle].

characterized by short distances while larger distances are found for CT excitations.

The formation of HLCT state can be analysed computationally by using excitation energies of LE and CT states (Scheme S2 and Table S2†). Due to extended π-conjugation in MPPIS-TPA, the CT state is stabilised than LE state and the reduced energy gap leading to full hybridisation of LE and CT states which inturn improves the OLED efficiency. However, in MPPIS-Cz the LE state is stabilised than CT state and the energy gap is high when compared with MPPIS-TPA results partial hybridisation (Scheme S2†). The overlap between hole and particle of MPPIS-Cz and MPPIS-TPA is displayed in Fig. S1.† Further, the composition of HLCT can also analysed computationally from the wave function of electron–hole pairs transition density matrix (TDM) and plot them in two dimension colour-filled map (Fig. S2 and S3†). The axes represent the atom in a molecule which is related to the probability of finding the electron and hole in the atomic orbitals localized on each non-hydrogen atom: the diagonal part represents the LE component localized on the main backbone while the off-diagonal region denotes the CT component. This further supports that the HLCT state also contributes to the hybridization apart from LE and CT states.[27] Upon excitation the electron is transferred from the donor and localized on the acceptor. Depending upon the intramolecular geometrical and electronic coupling the transferred electron is delocalized from the region of the nearby donor molecule to the vicinity of the acceptor. This effect can be qualitatively studied by the analysis of the density distribution at the ground and the excited states.[28,29]

Computed electron–hole properties, transition density and distance between hole and electron ($D_{\mathrm{H-E}}$), RMSD of electron and hole, *H* and *t* indices of MPPIS-Cz and MPPIS-TPA are displayed in Tables S3 and S4.† The integral value of hole and electron of MPPIS-Cz is less than that of MPPIS-TPA and the integral overlap of hole electron distribution ($S_{\mathrm{H-E}}$) is a measure of spatial separation of hole and electron. The $S_{\mathrm{H-E}}$ and $D_{\mathrm{H-E}}$ values supports the existence of LE and CT states. When compared with MPPIS-TPA, MPPIS-Cz has small $D_{\mathrm{H-E}}$ and high $S_{\mathrm{H-E}}$ values which indicates the charge transfer (CT) is higher in percentage for MPPIS-TPA isomer (Table S3†). RMSD of hole or electron characterizes the charge transfer distribution breadth. Table S4† show that the RMSD of MPPIS-Cz is higher in *X* direction for S_1–S_5 states which indicates the electron and hole distribution is much broader in *X* direction. The similar trend is observed for MPPIS-TPA but the total RMSD of hole and electron is higher for MPPIS-Cz than MPPIS-TPA. Table S5† summarises D_{CT}, q_{CT}, μ_{CT}, barycenter of charges (R_+ and R_-) and two CT indexes (*H* and *t*). The D_{CT} of MPPIS-Cz and MPPIS-TPA is calculated to be 0.459 and 0.607, respectively (Fig. 5). Distance between centroid of hole and electron (D_{CT}) is a measure of CT length: larger the D_{CT}, longer length is the charge transfers in the MPPIS-Cz and MPPIS-TPA. The CT length measures the distance between the barycenters (D_{CT}) and the transferred charges (q_{CT}) by the integration of the density depletion functions. The *H* index measures the spread of the positive and negative regions related to CT and *t* index is the difference between D_{CT} and H index (eqn (S15) and (S16)†). For both MPPIS-Cz and MPPIS-TPA, *t* is greater than zero and it is

Open Access Article. Published on 28 February 2017. Downloaded on 2/17/2026 6:30:33 PM.
This article is licensed under a Creative Commons Attribution 3.0 Unported Licence.

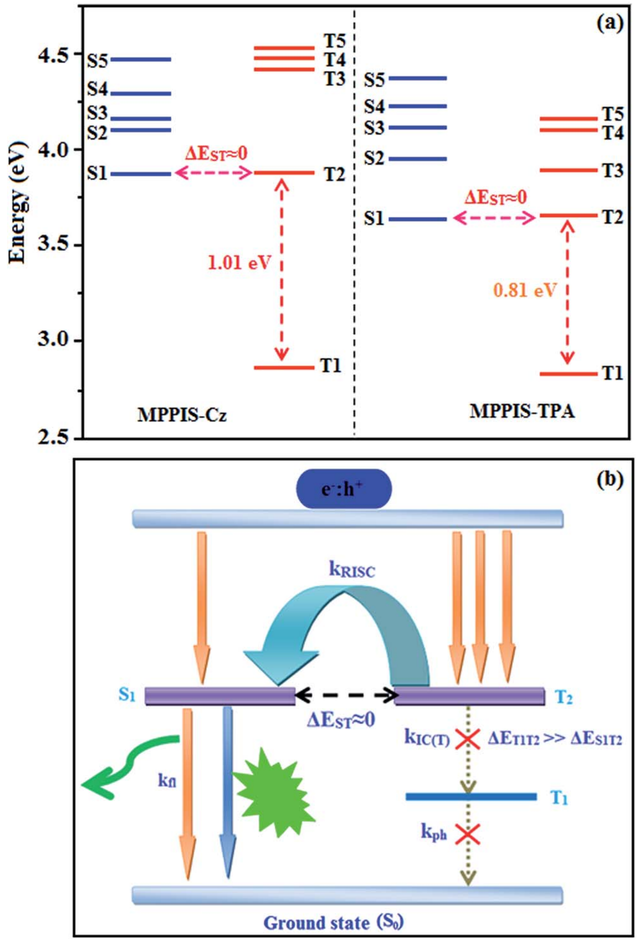

Fig. 4 (a) Energy level of singlet (S) and triplet (T) states of MPPIS-Cz and MPPIS-TPA; (b) scheme of exciton decay process after hole and electron recombination in OLEDs of twisting D–π–A molecules.

negative in all directions. This reveals that the overlap of hole and electron is very severe. Using the total electron density computed for the ground and excited states, it is possible to evaluate $\Delta\rho$, ρ_+, and ρ_- on a grid points around MPPIS-Cz and MPPIS-TPA (eqn (S2)–(S4),† Fig. 5). The green and blue zones corresponding to the centroids of charges (eqn (S9) and (S10)†) ρ_+ and ρ_-, respectively: the density depletion (blue) zones are mostly located on the TPA and Cz donor groups and the regions of density increment (green) are localized on the acceptor phenanthrimidazole moiety. The barycenter of charges (R_+ and R_-) are calculated according to the eqn (S5) and (S6):† R_- barycenter is close to the pheanthrimidazole group and R_+ barycenter is close to Cz and TPA. The computed change in dipolemoment (μ_{CT}) between the ground and excited states is determined using D_{CT} and q_{CT} (eqn (S8)†). The computed overlap between the ρ_+ and ρ_- regions for MPPIS-Cz and MPPIS-TPA as 0.9939 and 0.9795, respectively (Table S5†).

3.2. Electrochemical, thermal and photophysical properties

From the cyclic voltammogram of MPPIS-Cz and MPPIS-TPA, the HOMO and LUMO energies have been calculated (Fig. 6a). The LUMO energies of both MPPIS-Cz (−2.73 eV) and MPPIS-TPA (−2.69 eV) are nearly same which is attributed to their same acceptor MPPIS unit. The HOMO energy −5.34 eV of MPPIS-Cz is lower than that of MPPIS-TPA (−5.19 eV) corresponding to that of Cz and TPA group, respectively. The decreased HOMO energy of MPPIS-Cz is due to the poor electron donating ability of Cz relative to TPA and this observation was supported by DFT calculation. The thermal properties of blue light emitting materials (MPPIS-Cz and MPPIS-TPA) have been analysed to understand the device stability. For MPPIS-Cz, the glass transition temperature (T_g) and thermal decomposition temperature (T_d) were measured as 156 and 438 °C which are higher than that of MPPIS-TPA (T_g – 128 and T_d – 426 °C) (Fig. 6b). The higher thermal stability of MPPIS-Cz is due to the

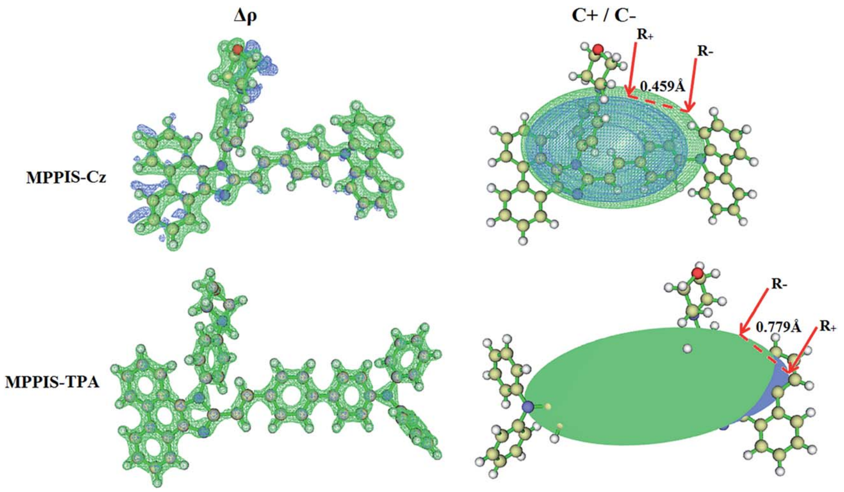

Fig. 5 Computed difference in total density for ground and excited states [$\Delta\rho(r) = \rho_{Ex}(r) - \rho_{Gs}(r)$; isosurface value for MPPIS-Cz (0.0500 a.u) and for MPPIS-TPA (0.0010 a.u)]; graphical representation of D_{CT} and centroids of charges [$C_+(r)/C_-(r)$; isosurface value for MPPIS-Cz (0. 29 a.u) and for MPPIS-TPA (0.1 a.u)].

Open Access Article. Published on 28 February 2017. Downloaded on 2/17/2026 6:30:33 PM.
This article is licensed under a Creative Commons Attribution 3.0 Unported Licence.

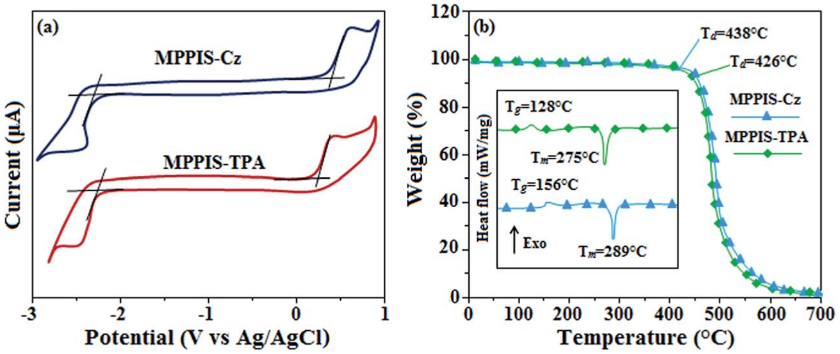

Fig. 6 (a) Cyclic voltammogram of MPPIS-Cz and MPPIS-TPA; (b) DSC and TGA graphs of MPPIS-TPA and MPPIS-Cz.

stronger rigidity of Cz than TPA which will be in favour of OLED stability.

UV-vis spectra show the absorption peak at 328 and 350 nm for MPPIS-Cz and MPPIS-TPA, respectively and their emission maxima was observed at 420 and 444 nm in dichloromethane solution (Fig. 7a). Compared with MPPIS-TPA, MPPIS-Cz exhibit blue shift for both UV-vis (22 nm) and PL (24 nm) which can be attributed to the poor electron donor ability of Cz relative to TPA results an increased LE component with simultaneous decrease of CT component in S_1 emissive state. The full width at half maximum in absorption spectrum of MPPIS-Cz (40 nm) is narrowed relative to that of MPPIS-TPA (50 nm). This observation also indicates that the decrease of CT component in S_1 state of MPPIS-Cz which is in good agreement with NTO description for $S_0 \rightarrow S_1$ transition. Furthermore, both UV-vis and PL spectra of MPPIS-Cz and MPPIS-TPA have been measured in vacuum evaporated film. UV-vis and PL spectra of MPPIS-Cz in solid film (UV – 320 nm; PL – 436 nm) show a significant blue shift when compared with MPPIS-TPA (UV – 342; PL – 446 nm). The larger twist angle of θ_1 in the ground state of MPPIS-Cz may weaken the intermolecular interactions and decrease the molecular aggregation results increase of photoluminance efficiency ($\eta_{\rm PL}$) through the suppression of aggregation induced fluorescence quenching.[30a]

The intramolecular charge transfer of both MPPIS-Cz and MPPIS-TPA in excited states have been analysed by solvatochromic effect.[13,14] The fluorescence of MPPIS-Cz exhibits solvatochromic effect with increase of solvent polarity and the total red shift of 70 nm is smaller than that of MPPIS-TPA (90 nm) (Fig. S4†). Similarly a small shift of 15 nm and 18 nm for MPPIS-Cz and MPPIS-TPA, respectively, has been observed in the absorption spectra (Fig. S4†). The solvatochromic shifts reveal that the low lying excited state S_1 of the MPPIS-Cz and MPPIS-TPA must possesses certain CT state character.[30,31] The percentage of CT character in S_1 state of MPPIS-Cz is lower than that in MPPIS-TPA and the percentage of LE character for MPPIS-Cz is higher than that in MPPIS-TPA. The quantum yield of MPPIS-TPA ($\phi_{\rm sol/film}$: 0.71/0.60) is higher than that of MPPIS-Cz ($\phi_{\rm sol/film}$: 0.61/0.58) as a result of the enhanced LE component in emissive state. A similar trend is observed from low polar to high polar solvent indicates the less percentage of CT in MPPIS-Cz than that in MPPIS-TPA.

The excited state dipole moment (μ_e) of MPPIS-Cz and MPPIS-TPA have been calculated from the Lippert–Mataga plot of Stokes shift ($\nu_a - \nu_f$) against orientation polarizability, $f(\varepsilon,n)$ (Fig. 7b) (Tables S6 and S7†).[32] Both compounds show two independent slopes of two section fitted lines which reveal the existence of two different characters of excited state.[33] The dipolemoment was calculated to be 24.9 (R^2 – 0.87) and 9.9D (R^2 – 0.91) (MPPIS-Cz) and 23.8 (R^2 – 0.96) and 12.1D (R^2 – 0.87) (MPPIS-TPA) for high and low polar solvents, respectively. In low-polar solvents, the dipole moment of 9.9D (MPPIS-Cz) and 12.1D (MPPIS-TPA) reveal that the S_1 state possessed CT character in addition to LE. The quantum yield of both MPPIS-Cz

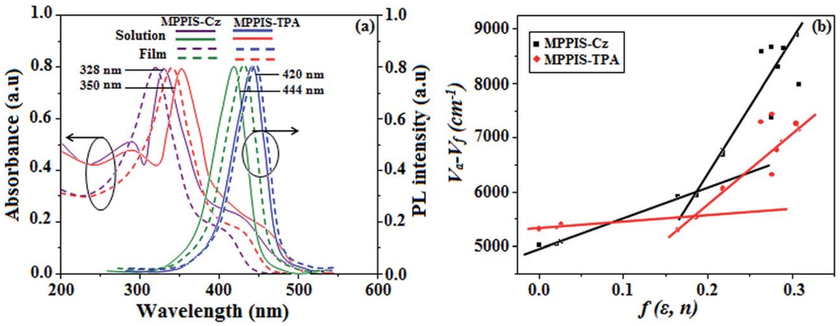

Fig. 7 (a) Normalized absorption and emission spectra of MPPIS-Cz and MPPIS-TPA in dichloromethane and film; (b) Lippert–Mataga plot of MPPIS-Cz and MPPIS-TPA in different solvents.

Open Access Article. Published on 28 February 2017. Downloaded on 2/17/2026 6:30:33 PM.
This article is licensed under a Creative Commons Attribution 3.0 Unported Licence.

and MPPIS-TPA decreases with increasing solvent polarity and relatively high quantum yield was obtained between hexane and butyl ether. These factors demonstrated that certain degree of locally excited (LE) character has been introduced thus, S_1 state in low polar solvents contained both CT and LE components. However, observation of single-exponential fluorescence decay (Fig. 8a) for MPPIS-Cz and MPPIS-TPA in low polar solvents reveal that a new and unique excited state *i.e.*, hybridized local and charge-transfer (HLCT) state exists in the D–π–A architecture rather than a mixture of LE and CT states.[34,35] In low polarity solvent, the smaller μ_e of MPPIS-Cz relative to MPPIS-TPA can be ascribed to weak donor ability of Cz than TPA corresponding to the higher LE proportion as expected in molecule design of MPPIS-Cz.

The two section linear relation between Stokes shift and solvent polarity indicating that both MPPIS-Cz and MPPIS-TPA possess an intercrossed excited state of LE and CT: a higher contribution from CT state in high polarity solvents ($f \geq 0.2$), whereas a dominant contribution from LE state in low polarity solvents ($f \leq 0.1$). The intercrossed excited state of the LE and CT may occur in a moderate polarity between butyl ether and ethyl acetate. The hybridized local and charge transfer (HLCT) state forms due to the intercrossing coupling between LE and CT states. The lifetime measurement reveals that this intercrossed excited state in different polar solvents should be a hybridized local and charge transfer state (HLCT) instead of two species state through a simple addition of LE and CT (Scheme S2†).

The time correlated single photon counting (TCSPC) results fit to mono exponential decay, $f(t) = a\exp(-t/\tau)$, where α and τ are respectively, the pre-exponential factor and lifetime of the various excited states involved. If N_i molecules are excited at zero time, the quantum yield of the i_{th} component α_i is proportional to the ratio $\alpha_i\tau_i/N_i$ and the α_i factors are related to the absorbance of the various substances at the excitation wavelength. Laser excitation was set at 270 nm and the fluorescence signal was measured at emission wavelength of individual compound. DAS6 software was used for the fit and the χ^2 values are less than 1.2. The mono exponential lifetime demonstrates that the intercrossed LE and CT in the moderate polarity solvent formed as one hybridized HLCT state which supports the molecular design (Fig. 8a). The emission wavelength of both MPPIS-Cz and MPPIS-TPA in film is close to that in ethyl ether which supports the HLCT state formed in MPPIS-Cz and MPPIS-TPA film. The radiative transition rate (k_r) and the non-radiative transition rate (k_{nr}) of MPPIS-Cz and MPPIS-TPA have been calculated from lifetime and quantum yield. Compared with MPPIS-TPA, the k_r of MPPIS-Cz is increased and k_{nr} of MPPIS-Cz is decreased (Fig. S5†). This result is also in good agreement with the aim of our molecular design.

Table 1 Device performances of MPPIS-Cz and MPPIS-TPA[a]

Parameters	MPPIS-Cz	MPPIS-TPA
V_{1000} (V)	5.2	6.1
L (cd m^{-2})	4801	3858
η_{ex} (%)	1.48	1.34
η_c (cd A^{-1})	1.52	1.46
η_p (lm W^{-1})	1.30	1.28
EL (nm)	430	435
CIE (x, y)	0.16, 0.08	0.15, 0.12
η_{IQE} (%)[b]	7.4	6.7
η_s (%)[c]	11.7	11.6

[a] η_c – luminous efficiency; η_p – power efficiency; η_{EQE} – external quantum efficiency; EL – electroluminescence. [b] η_{IQE} – maximum internal quantum efficiency; ($\eta_{IQE} = \eta_{EQE}/\eta_{out}$). [c] η_s – light out coupling efficiency (η_{IQE}/η_{PL}).

3.3. Electroluminescence properties

The effective film formatting properties of light emitting materials are important for device efficiency. The surface morphologies of vacuum deposited thin film of MPPIS-Cz and MPPIS-TPA have been studied by atomic force microscopy (AFM) topography images and the root-mean-square (RMS) roughness is 0.31 and 0.38 nm, respectively. The thin film of MPPIS-Cz exhibit lowest RMS which results high efficiency (Fig. 8b). To evaluate the EL performances of MPPIS-Cz and MPPIS-TPA, non-doped OLEDs were fabricated with

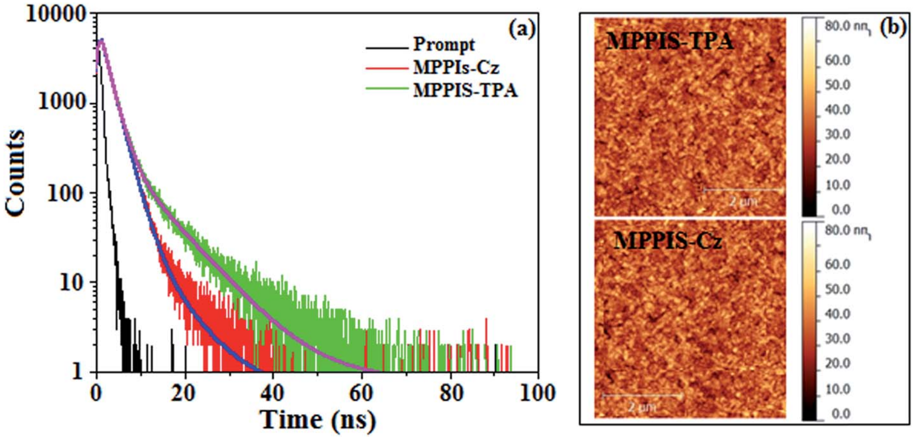

Fig. 8 (a) Lifetime decay curve; (b) AFM images based film at room temperature of MPPIS-Cz and MPPIS-TPA.

Open Access Article. Published on 28 February 2017. Downloaded on 2/17/2026 6:30:33 PM.
This article is licensed under a Creative Commons Attribution 3.0 Unported Licence.

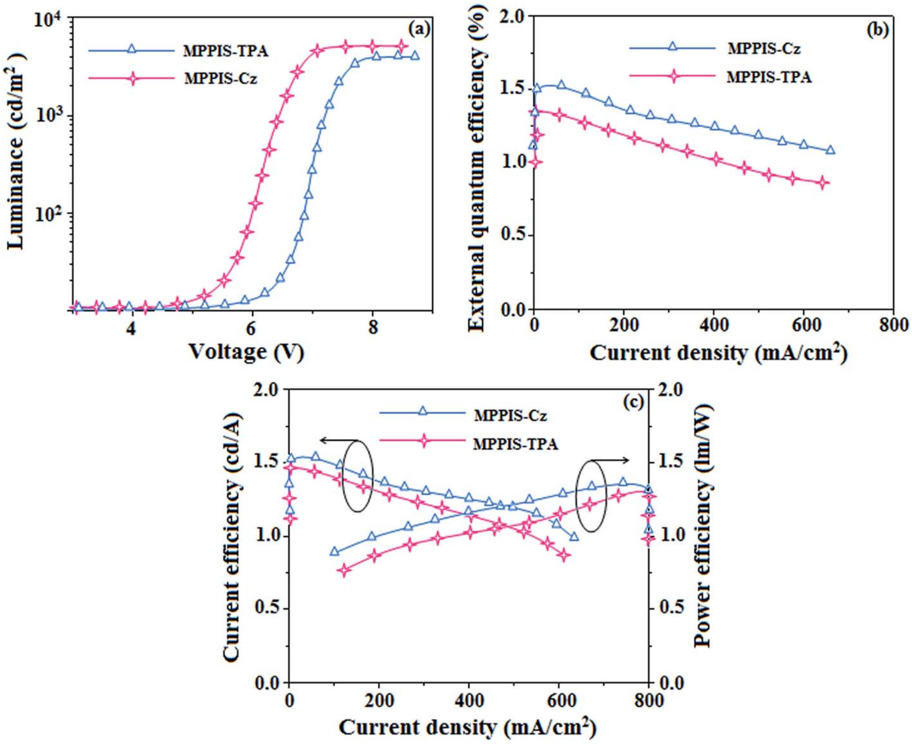

Fig. 9 Electroluminescence performances: (a) luminance *versus* voltage; (b) external quantum efficiency *versus* current density; (c) current efficiency and power efficiency *versus* current density of non-doped EL device with MPPIS-TPA and MPPIS-Cz as emitter.

a device structure: ITO/*N*,*N*′-di-1-naphthyl-*N*,*N*′-diphenylbenzidine (NPB) (70 nm)/MPPIS-Cz or MPPIS-TPA (20 nm)/1,3,5-tri(phenyl-2-benzimidazolyl)-benzene (TPBi) (20 nm)/LiF (0.5 nm)/Al (100 nm). Compared with MPPIS-TPA, MPPIS-Cz based device shows a maximum luminous efficiency of 1.52 cd A^{-1} and maximum luminance of 4801 cd m^{-2}. Based on the external quantum efficiency-luminance characteristics of the two devices, the MPPIS-Cz device harvests a maximum external quantum efficiency of 1.48% and power efficiency of 1.30 lm W^{-1} (Table 1; Fig. 9). The calculated internal quantum efficiency (η_{IQE}) of MPPIS-Cz and MPPIS-TPA are to be 7.4% and 6.7%, respectively and the exciton utilisation efficiency are to be 12.3% and 11.6%, respectively. The current and power efficiencies of the devices based on MPPIS-Cz (1.52 cd A^{-1}; 1.30 lm W^{-1}) and MPPIS-TPA (1.46 cd A^{-1}; 1.28 lm W^{-1}) are higher than those of the devices based on TPA-PA (1.16 cd A^{-1}; 0.65 lm W^{-1}), TPA-NzP (1.00 cd A^{-1}; 0.77 lm W^{-1})[19] and *m*TPA-PPI (0.84 cd A^{-1}; 0.48 lm W^{-1}).[19b] Also the external quantum yield of MPPIS-Cz (71%) and MPPIS-TPA (61%) are higher than those of (i) Cz-BzP (69.7%) and TPA-BzP (49.2%)[30a] (ii) CBI (21%) and MCB (24%)[19c] and (iii) PPI-pCNCz (54%).[30b] Wang *et al.*,[30c] report that the thickness of the LBPPI emissive layer alters the current efficiency (50 nm – 0.01 cd A^{-1}; 40 nm – 0.13 cd A^{-1}; 30 nm – 0.40 cd A^{-1} and 20 nm – 0.68 cd A^{-1}).[32d] The current efficiency obtained in the present study with thickness of 20 nm of MPPIS-Cz (1.52 cd A^{-1}) and 20 nm of MPPIS-TPA (1.46 cd A^{-1}) is higher than those reported by Wang *et al.* Hence it is possible to improve the efficiency of these materials through modification of thickness of the emissive layer. Effort will be made to modify the thickness of the emissive layer to enhance the efficiency and also effort will made to increase the radiative rate in future of our studies. The weaker donor carbazole substituted phenanthrimidazole exhibit current efficiency of 0.88 cd A^{-1} and power efficiency of 0.30 lm W^{-1} (ref. 32*e*) and Gao *et al.*, reported carbazole substituted compound with current efficiency of 0.65 cd A^{-1} and 0.48 lm W^{-1}.[32c] These carbazole substituted compound exhibit less efficiencies than those obtained in our studies MPPIS-Cz (1.52 cd A^{-1}; 1.30 lm W^{-1}) and MPPIS-TPA (1.46 cd A^{-1}; 1.28 lm W^{-1}). The device efficiency indicates that MPPIS-Cz is one of the best fluorescent OLEDs materials.

4. Conclusion

We have synthesized fluorescent D–π–A molecules, MPPIS-Cz and MPPIS-TPA possess HLCT state to obtain maximum EL efficiency through high PL efficiency and high exciton utilization in fluorescent OLED. The photophysical, film morphology and electrochemical properties of MPPIS-Cz and MPPIS-TPA can be tuned by chemical modification from MPPIS-TPA to MPPIS-Cz by changing the strong donor TPA moiety by weak donor Cz moiety. This results HLCT as the emissive state with increased LE and decreased CT which in turn increased the quantum efficiency. The external quantum efficiency of non-doped device based on MPPIS-Cz is 1.48% and its radiative rate is 12.2 × 10^6 s^{-1}. This is probably as a result of efficient RISC ($T_2 \rightarrow S_1$) through hot exciton process. The MPPIS-Cz based non-doped fluorescent OLED show a CIE coordinates of (0.16, 0.08), maximum current efficiency of 1.52 cd A^{-1},

Open Access Article. Published on 28 February 2017. Downloaded on 2/17/2026 6:30:33 PM.
This article is licensed under a Creative Commons Attribution 3.0 Unported Licence.

maximum external quantum efficiency of 1.48% and power efficiency 1.30 lm W^{-1}. These results are helpful to design the next generation efficient low cost fluorescent OLED materials using HLCT state principle and hot exciton model.

Acknowledgements

One of the author Dr J. Jayabharathi thank Department of Science and Technology (EMR/2014/000094), Defence Research and Development Organization (213/MAT/10-11), Council of Scientific and Industrial Research [No. 01/(2707)/13EMR-II], University Grant Commission (36-21/2008) and Nano Mission (SR/NM/NS-1001/2016) for financial support.

References

1 (*a*) C. Chein, C. Chen, F. Hsu, C. Shu, P. Chou and C. Lai, *Adv. Funct. Mater.*, 2009, **19**, 560–566; (*b*) C. H. Chang, M. C. Kuo, W. C. Lin, Y. T. Chen, K. T. Wong, S. H. Chou, E. Mondal, R. C. Kwong, S. Xia, T. Nakagawa and C. Adachi, *J. Mater. Chem.*, 2012, **22**, 3832–3838.

2 D. H. Kim, N. S. Cho, H. Y. Oh, J. H. Yang, W. S. Jeon, J. S. Park, M. C. Suh and J. H. Kwon, *Adv. Mater.*, 2011, **23**, 2721–2726.

3 (*a*) H. Fukagawa, T. Shimizu, H. Hanashima, Y. Osada, M. Suzuki and H. Fujikake, *Adv. Mater.*, 2012, **24**, 5099–5103; (*b*) Y. Cho and J. Lee, *Adv. Mater.*, 2011, **23**, 4568–4572.

4 (*a*) M. T. Lee, H. H. Chen, C. H. Liao, C. H. Tsai and C. H. Chen, *Appl. Phys. Lett.*, 2004, **85**, 3301–3303; (*b*) M. T. Lee, C. H. Liao, C. H. Tsai and C. H. Chen, *Adv. Mater.*, 2005, **17**, 2493–2497.

5 (*a*) A. Kraft, A. C. Grimsdale and A. B. Holmes, *Angew. Chem., Int. Ed.*, 1998, **37**, 402–428; (*b*) H. Sasabe, N. Toyota, H. Nakanishi, T. Ishizaka, Y. J. Pu and J. Kido, *Adv. Mater.*, 2012, **24**, 3212–3217; (*c*) H. Huang, Y. X. Wang, S. Q. Zhuang, X. Yang, L. Wang and C. L. Yang, *J. Phys. Chem. C*, 2012, **116**, 19458–19466.

6 J. Hu, Y. Pu, F. Satoh, S. Kawata, H. Katagiri, H. Sasabe and J. Kido, *Adv. Mater.*, 2014, **24**, 2064–2071.

7 T. C. Chao, Y. T. Lin, C. Y. Yang, T. S. Hung, H. C. Chou, C. C. Wu and K. T. Wong, *Adv. Mater.*, 2005, **17**, 992–996.

8 J. R. Sheats, H. Antoniadis, M. Hueschen, W. Leonard, J. Miller, R. Moon, D. Roitman and A. Stocking, *Science*, 1996, **273**, 884–888.

9 (*a*) H. Uoyama, K. Goushi, K. Shizu, H. Nomura and C. Adachi, *Nature*, 2012, **492**, 234–235; (*b*) Q. Zhang, B. Li, S. Huang, H. Nomura, H. Tanaka and C. Adachi, *Nat. Photonics*, 2014, **8**, 326–332; (*c*) H. Tanaka, K. Shizu, H. Miyazaki and C. Adachi, *Chem. Commun.*, 2012, **48**, 11392–11394; (*d*) Q. Zhang, J. Li, K. Shizu, S. Huang, S. Hirata, H. Miyazaki and C. Adachi, *J. Am. Chem. Soc.*, 2012, **134**, 14706–14709.

10 S. P. Jagtap, S. Mukhopadhyay, V. Coropceanu, G. L. Brizius, J. Bredas and D. M. Collard, *J. Am. Chem. Soc.*, 2012, **134**, 7176–7185.

11 Z. R. Grabowski, K. Rotkiewicz and W. Rettig, *Chem. Rev.*, 2003, **103**, 3899–4031.

12 S. Zhang, L. Yao, Q. Peng, W. Li, Y. Pan, R. Xiao, Y. Gao, C. Gu, Z. Wang, P. Lu, F. Li, S. Su, B. Yang and Y. Ma, *Adv. Funct. Mater.*, 2015, **25**, 1755–1762.

13 W. J. Li, D. D. Liu, F. Z. Shen, D. G. Ma, Z. M. Wang, T. Fei, B. Yang and Y. G. Ma, *Adv. Funct. Mater.*, 2012, **22**, 2797–2803.

14 W. J. Li, Y. Y. Pan, R. Xiao, Q. M. Peng, S. T. Zhang, D. G. Ma, F. Li, F. Z. Shen, Y. H. Wang, B. Yang and Y. G. Ma, *Adv. Funct. Mater.*, 2014, **24**, 1609–1614.

15 S. Tang, W. J. Li, F. Z. Shen, D. D. Liu, B. Yang and Y. G. Ma, *J. Mater. Chem.*, 2012, **22**, 4401–4408.

16 S. T. Zhang, W. J. Li, L. Yao, Y. Y. Pan, B. Yang and Y. G. Ma, *Chem. Commun.*, 2013, **49**, 11302–11304.

17 L. Yao, S. T. Zhang, R. Wang, W. J. Li, F. Z. Shen, B. Yang and Y. G. Ma, *Angew. Chem., Int. Ed.*, 2014, **126**, 2151–2155.

18 Y. Y. Pan, W. J. Li, S. T. Zhang, L. Yao, C. Gu, H. Xu, B. Yang and Y. G. Ma, *Adv. Opt. Mater.*, 2014, **2**, 510–515.

19 (*a*) W. J. Li, Y. Y. Pan, L. Yao, H. C. Liu, S. T. Zhang, C. Wang, F. Z. Shen, B. Yang and Y. G. Ma, *Adv. Opt. Mater.*, 2014, **2**, 892–910; (*b*) H. Liu, Q. Bai, L. Yao, H. Zhang, H. Xu, S. Zhang, W. Li, Y. Gao, J. Li, P. Lu, H. Wang, B. Yang and Y. Mac, *Chem. Sci.*, 2015, **6**, 3797–3804; (*c*) N. Nagarajan, G. Velmurugan, G. Prabhu, P. Venuvanalingam and R. Renganathan, *J. Lumin.*, 2014, **147**, 111–120.

20 D. Chaudhuri, E. Sigmund, A. Meyer, L. Rcck, P. Klemm, S. Lautenschlager, A. Schmid, S. R. Yost, T. Van, S. Bange, S. Hcger and J. M. Lupton, *Angew. Chem.*, 2013, **125**, 13691–13694.

21 M. A. Baldo, S. Lamansky, P. E. Burrows, M. E. Thompson and S. R. Forrest, *Appl. Phys. Lett.*, 1999, **60**, 14422–14428.

22 T. Forster, 10th Spiers Memorial Lecture, *Discuss. Faraday Soc.*, 1959, **27**, 7–17.

23 (*a*) M. J. Frisch, G. W. Trucks, H. B. Schlegel, G. E. Scuseria, M. A. Robb, J. R. Cheeseman, J. A. Montgomery, T. Vreven, K. N. Kudin, J. C. Burant, J. M. Millam, S. S. Iyengar, J. Tomasi, V. Barone, B. Mennucci, M. Cossi, G. Scalmani, N. Rega, G. A. Petersson, H. Nakatsuji, M. Hada, M. Ehara, K. Toyota, R. Fukuda, J. Hasegawa, M. Ishida, T. Nakajima, Y. Honda, O. Kitao, H. Nakai, M. Klene, X. Li, J. E. Knox, H. P. Hratchian, J. B. Cross, V. Bakken, C. Adamo, J. Jaramillo, R. Gomperts, R. E. Stratmann, O. Yazyev, A. J. Austin, R. Cammi; C. Pomelli, J. W. Ochterski, P. Y. Ayala, K. Morokuma, G. A. Voth, P. Salvador, J. J. Dannenberg, V. G. Zakrzewski, S. Dapprich, A. D. Daniels, M. C. Strain, O. Farkas, D. K. Malick, A. D. Rabuck, K. Raghavachari, J. B. Foresman, J. V. Ortiz, Q. Cui, A. G. Baboul, S. Clifford, J. Cioslowski, B. B. Stefanov, G. Liu, A. Liashenko, P. Piskorz, I. Komaromi, R. L. Martin, D. J. Fox, T. Keith, M. A. Al-Laham, C. Y. Peng, A. Nanayakkara, M. Challacombe, P. M. W. Gill, B. Johnson, W. Chen, M. W. Wong, C. Gonzalez and J. A. Pople, *Gaussian 03 (Revision E.01)*, Gaussian, Inc., Wallingford, CT., 2004; (*b*) T. Lu and F. Chen, *J. Comput. Chem.*, 2012, **33**, 580–592.

24 (*a*) Y. Zhang, S. L. Lai, Q. X. Tong, M. F. Lo, T. W. Ng, M. Y. Chan, Z. C. Wen, J. He, K. S. Jeff, X. L. Tang, W. M. Liu, C. C. Ko, P. F. Wang and C. S. Lee, *Chem.*

Open Access Article. Published on 28 February 2017. Downloaded on 2/17/2026 6:30:33 PM.
This article is licensed under a Creative Commons Attribution 3.0 Unported Licence.

Mater., 2012, **24**(1), 61–70; (*b*) R. Kim, S. Lee, K. H. Kim, Y. J. Lee, S. K. Kwon, J. J. Kim and Y. H. Kim, *Chem. Commun.*, 2013, **49**, 4664–4666.

25 M. R. Zhu and C. L. Yang, *Chem. Soc. Rev.*, 2013, **42**, 4963–4976.

26 H. H. Chou, Y. H. Chen, H. P. Hsu, W. H. Chang, Y. H. Chen and C. H. Cheng, *Adv. Mater.*, 2012, **24**, 5867–5871.

27 J. Liu, Y. Zhang and W. Liu, *J. Chem. Theory Comput.*, 2014, **10**, 2436–2448.

28 J. Fortage, C. Peltier, F. Nastasi, F. Puntoriero, F. Tuyeres, S. Griveau, F. Bedioui, S. Campagna and P. P. Laine, *J. Am. Chem. Soc.*, 2010, **132**, 16700–16713.

29 C. Peltier, C. Adamo, P. P. Laine, S. Campagana, F. Punteriero and I. Ciofini, *J. Phys. Chem. A*, 2010, **114**, 8434–8443.

30 (*a*) C. Wang, X. Li, Y. Pan, S. Zhang, L. Yao, Q. Bai, W. Li, P. Lu, B. Yang, S. J. Su and Y. Ma, *ACS Appl. Mater. Interfaces*, 2016; (*b*) B. Wang, X. Lv, J. Tan, Q. Zhang, Z. Huang, W. Yi and L. Wang, *J. Mater. Chem. C*, 2016, **4**, 8473–8482; (*c*) Z. Wang, P. Lu, S. Chen, Z. Gao, F. Shen, W. Zhang, Y. Xu, H. S. Kwok and Y. Ma, *J. Mater. Chem.*, 2011, **21**, 5451–5456; (*d*) Y. Zou, J. H. Zou, T. L. Ye, H. Li, C. L. Yang, H. B. Wu, D. G. Ma, J. G. Qin and Y. Cao, *Adv. Funct. Mater.*, 2013, **23**, 1781–1788.

31 C. Liu, Q. Fu, Y. Zou, C. L. Yang, D. G. Ma and J. G. Qin, *Chem. Mater.*, 2014, **26**, 3074–3083.

32 (*a*) Z. Wang, P. Lu, S. Chen, Z. Gao, F. Shen, W. Zhang, Y. Xu, H. S. Kwok and Y. Ma, *J. Mater. Chem.*, 2011, **21**, 5451–5456; (*b*) H. Huang, Y. Wang, B. Wang, S. Zhuang, B. Pan, X. Yang, L. Wang and C. Yang, *J. Mater. Chem. C*, 2013, **1**, 5899–5907; (*c*) Z. Gao, Y. Liu, Z. Wang, F. Shen, H. Liu, G. Sun, L. Yao, Y. Lv, P. Lu and Y. Ma, *Chem.–Eur. J.*, 2013, **19**, 2602–2605; (*d*) Z. Wang, Y. Feng, H. Li, Z. Gao, X. Zhang, P. Lu, P. Chen, Y. Ma and S. Liu, *Phys. Chem. Chem. Phys.*, 2014, **16**, 10837–10843; (*e*) Z. Gao, Z. Wang, T. Shan, Y. Liu, F. Shen, Y. Pan, H. Zhang, X. He, P. Lu, B. Yang and Y. Ma, *Org. Electron.*, 2014, **15**, 2667–2676; (*f*) Z. Gao, G. Cheng, F. Shen, S. Zhang, Y. Zhang, P. Lu and Y. Ma, *Laser Photonics Rev.*, 2014, **8**, L6–L10.

33 (*a*) V. E. Z. Lippert, *Electrochemistry*, 1957, **61**, 962–975; (*b*) N. Mataga, Y. Kaifu and M. Koizumi, *Bull. Chem. Soc. Jpn.*, 1956, **29**, 465–470.

34 (*a*) C. J. Chiang, A. Kimyonok, M. K. Etherington, G. C. Griffiths, V. Jankus, F. Turksoy and A. P. Monkman, *Adv. Funct. Mater.*, 2013, **23**, 739–746; (*b*) D. Y. Kondakov, T. D. Pawlik, T. K. Hatwar and J. P. Spindler, *J. Appl. Phys.*, 2009, **106**, 124510–124517.

35 R. L. Martin, *J. Chem. Phys.*, 2003, **118**, 4775–4777.

This journal is © The Royal Society of Chemistry 2017